Quench-drive spectroscopy and high-harmonic generation in BCS superconductors

Matteo Puviani [1,2,*] Rafael Haenel [1,3,†] and Dirk Manske[1,‡]

[1]*Max Planck Institute for Solid State Research, 70569 Stuttgart, Germany*
[2]*Max Planck Institute for the Science of Light, 91058 Erlangen, Germany*
[3]*Department of Physics and Astronomy, Quantum Matter Institute, University of British Columbia, Vancouver,
British Columbia V6T 1Z4, Canada*

In pump-probe spectroscopies, THz pulses are used to quench a system, which is subsequently probed by either a THz or optical pulse. In contrast, third-harmonic generation experiments employ a single multicycle driving pulse and measure the induced third harmonic. In this work, we analyze a spectroscopy setup where both a quench and a drive are applied and two-dimensional spectra as a function of time and quench-drive delay are recorded. We calculate the time evolution of the nonlinear current generated in the superconductor within an Anderson-pseudospin framework and characterize all experimental signatures using a quasiequilibrium approach. We analyze the superconducting response in Fourier space with respect to both the frequencies corresponding to the real time and the quench-drive delay time. In particular, we show the presence of a transient modulation of higher harmonics, induced by a wave mixing process of the drive with the quench pulse, which probes both quasiparticle and collective excitations of the superconducting condensate.

I. INTRODUCTION

The superconducting state of matter is characterized by a variety of collective modes: These include, among others, Higgs, Leggett, bi-plasmon, and Bardasis-Schrieffer modes [1–11]. The study of these modes is currently being established as a new field of collective mode spectroscopy, in the sense that bosonic excitations of the condensate reveal information about the underlying superconducting ground state and symmetry properties of the condensate itself [7,10,12,13]. The Higgs mode, for instance, can be used as a spectroscopic tool to distinguish between different gap symmetries of unconventional superconductors [10].

The experimental study of collective superconducting modes poses significant challenges. Due to particle-hole symmetry, they generally cannot couple linearly to electromagnetic fields in the spatially homogeneous limit [3,14]. Instead, they are activated in a two-photon Raman-like process [15,16]. Thus, the main signature of collective modes consists of a renormalization of the nonlinear susceptibility, which can be probed by nonlinear spectroscopic techniques, such as high-harmonic generation, optical Kerr effect, and nonlinear optical conductivity measurements [17–19].

*matteo.puviani@mpl.mpg.de
†r.haenel@fkf.mpg.de
‡d.manske@fkf.mpg.de

Generally, two distinct approaches exist to excite collective oscillations of a superconductor: The first is to apply a short-duration quench pulse, $\tau\Delta < 1$ (τ being the pulse duration and Δ the energy gap), to suddenly shrink the superconducting gap and excite the system into an out-of-equilibrium state [10]. The second approach uses a single longer pulse, $\tau\Delta \gg 1$, to drive the material into a quasisteady excited state [10,18,20].

Higher-dimensional spectroscopy techniques have been used to study the nonlinear response of various materials [21–24], but they have rarely been applied to superconductors [25]. Instead, for superconductors, most time-resolved spectroscopies and theoretical studies have focused only on either short quench pulses or a multicycle driving pulse [5,26], without mixing them simultaneously. In the present work, we study the full evolution of the nonlinear current in the BCS superconducting state subjected to a spectroscopic setup where *both* a quench and a drive pulse are applied [Fig. 1(a)]. We show how the spectroscopic data can be clearly analyzed in two-dimensional (2D) Fourier space $(\omega, \omega_{\Delta t})$, where the two frequency variables correspond to conjugates of real time t and the pump probe delay Δt, respectively. While these spectra reduce to the aforementioned pump-probe and third-harmonic generation (THG) experiments in certain limits, we argue that quench-drive spectroscopy provides a comprehensive way to experimentally extract information of the nonlinear optical susceptibility and the spectrum of superconducting collective modes. We stress that one of the experimental advantages of the proposed quench-drive spectroscopy is that pulse frequencies need not be continuously scanned across a range of frequencies to probe the system, in contrast to simple driving protocols [27]. Instead, to achieve frequency resolution and collective mode resonance, only the
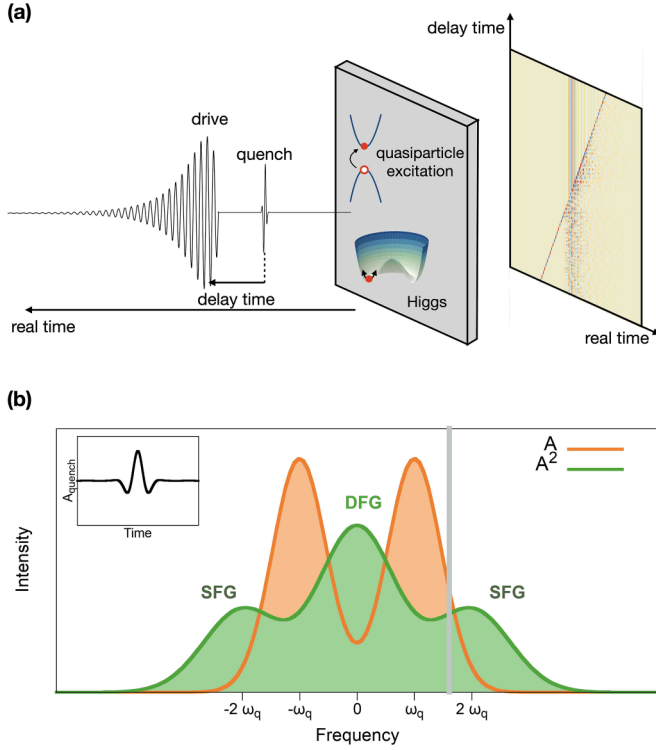
(a)

(b)

FIG. 1. Quench-drive spectroscopy. (a) Quench-drive spectroscopy setup. A single-cycle quench pulse and a multicycle drive pulse excite both Higgs mode and quasiparticles, resulting in a third-harmonic generation (THG) and a dynamical modulation of higher harmonics. In addition, the driving pulse effectively quenches the system, launching Higgs oscillations. In this illustration we show the asymmetric driving pulse. (b) Representation of the frequency spectrum of the quench pulse $A_q(\omega)$ (orange), centered at $\omega = \omega_q$, and the sum (SFG) and difference frequency generated (DFG) pulses $A^2(\omega)$ (green), centered at $\omega = 0$ and $\omega = 2\omega_q$, respectively. The grey vertical line represents the position of the critical value 2Δ. In the inset the real-time quench pulse is shown.

time delay between quench and drive pulses needs to be swept.

To solve the equations of motion for a superconductor we employ a pseudospin model, extended to describe the quench-drive setup. This allows for the simulation of the evolution of the order parameter as well a calculation of the current induced in the superconductor [3,7]. In addition, we present a diagrammatic approach to systematically interpret the two-dimensional spectra.

The paper is organized as follows: In Sec. II we introduce the quench-drive spectroscopy mechanism and explain its features diagrammatically. In Sec. III we describe the theoretical background. We use the pseudospin model to solve the Heisenberg equation of motion in the presence of an external field for the time-dependent order parameter, and then calculate the generated nonlinear current. In Sec, IV we show the numerical results of the nonlinear current for the quench-drive setup in a BCS superconductor. The discussion of results is provided in Sec. V. Finally, we give a summary and outlook on future applications and perspectives of quench-drive spectroscopy in Sec. VI.

II. QUENCH-DRIVE SPECTROSCOPY

We consider here a clean BCS superconductor without impurity scattering. We are interested in the nonlinear response of the superconductor, which is of third order in the external light field in materials with inversion symmetry. In particular, the quasiequilibrium third-order current is determined by the diamagnetic coupling to light, and its time-dependent expression reads [7,26,28]

$$j(t) = A(t)(\chi_{\rho\rho} * A^2)(t) \tag{1}$$

where $(B * C)(x) = \int dy\, B(y)C(x - y)$ denotes a convolution integral. The function $\chi_{\rho\rho}$ is the effective density-density response,

$$\chi_{\rho\rho}(t) = -i\theta(t)\langle[\rho(t), \rho(0)]\rangle, \tag{2}$$

of the operator $\rho = \sum_{\mathbf{k}\sigma} \frac{\partial^2 \epsilon_{\mathbf{k}}}{\partial k_x^2} c_{\mathbf{k}\sigma}^\dagger c_{\mathbf{k}\sigma}$. For ease of notation, we have assumed that all applied electromagnetic pulses are polarized along the **x** direction, i.e., $\mathbf{A} = A\,\hat{\mathbf{x}}$. In the general case, where **A** can have arbitrary polarization, the density-density response becomes a tensor whose structure encodes additional information about material properties. A specific case of cross-polarized pulses is discussed in Appendix C.

Within the BCS approximation, the gauge-invariant response for a single-band model has been computed in various references [3,15,26,28] and a general framework for pump-probe experiments based on a quasiequilibrium effective action formalism has been developed in Refs. [5,26]. The density-density response is found to be peaked at the resonance frequency 2Δ of the Higgs mode, where 2Δ is the single-particle superconducting spectral gap. It was pointed out, however, that the resonance peak in the density-density response is the result of both single-particle contributions, stemming from quasiparticle excitations, and collective mode excitations. Importantly, it was shown that quasiparticles generally give the dominating contribution to the 2Δ peak in the clean limit, making observation of the Higgs mode difficult [15]. Other collective modes of the condensate, such as Leggett [5,29,30], Bardasis-Schrieffer [9,31], or other relative phase modes [13] do contribute significantly to the density-density response and may even persist below the gap. Additionally, the Higgs modes may achieve a sizable signal in the presence of impurities [30,32–35] or due to additional processes [36,37]. In the present work, we will not focus on the attribution of spectral weight of the nonlinear response to their various origins and instead discuss spectroscopic measurement of the density-density response $\chi_{\rho\rho}$ as a whole.

In Fourier space Eq. (1) can be expressed as

$$j(\omega) = A * [\chi_{\rho\rho}(A * A)] = \int \prod_{i=1}^{3} d\omega_i\, \delta\left(\omega - \sum_i \omega_i\right)$$
$$\times A(\omega_1)\chi_{\rho\rho}(\omega_2 + \omega_3)A(\omega_2)A(\omega_3), \tag{3}$$

where the δ function is a manifestation of energy conservation, i.e., the three photon frequencies ω_i have to sum up to the frequency ω of the induced current.

The susceptibility $\chi_{\rho\rho}$ in Eq. (3) enters with a functional dependence on the frequency variables $\omega_2 + \omega_3$. In general,

the integration over these variables scrambles the resonance spectrum of $\chi_{\rho\rho}$ and no direct signature of collective modes can be recovered from $j(\omega)$.

Two approaches to circumvent this problem exist. First, one may choose A as a multicycle THz pulse of the form

$$A(t) = A_d(t) = A_d^0 \cos(\omega_d t + \phi) e^{-t^2/2\tau_d^2} \tag{4}$$

with $\tau_d \omega_d \gg 1$ and $\omega_d \sim \Delta$ such that it has a narrow frequency spectrum of width τ_d^{-1} centered around $\pm\omega_d$. Then, the integration variables are constrained to $\omega_i \approx \pm\omega_d$ and the susceptibilities are mostly evaluated at $\chi_{\rho\rho}(0)$ and $\chi_{\rho\rho}(\pm 2\omega_d)$ to yield the first or third harmonic, $j(\pm\omega_d)$ or $j(\pm 3\omega_d)$. To map out the functional dependence of $\chi_{\rho\rho}$ one has to vary the driving frequency ω_d. This, however, is not easily achievable experimentally. Instead, most current experiments fix the driving frequency ω_d and instead attempt to shift the resonance energies contained in $\chi_{\rho\rho}$. For a superconducting mode, this is simply achieved by varying the temperature in the window $(0, T_c)$. The clear disadvantages of this method are that (1) knowledge of the temperature dependence of the resonances of $\chi_{\rho\rho}$ is required, (2) only modes above $2\omega_d$ are visible, and (3) thermal broadening effects are substantial.

The second approach consists of a pump-probe setup. Here, we consider a pump-probe setup where, in addition to a broadband quench pulse A_q, the multicycle drive pulse A_d is utilized. The quench A_q has the same form as Eq. (4), but with $\tau_q \ll 1/\Delta$. Further details of the pulse shapes are given in Appendix B. The two pulses are delayed with respect to each other by Δt yielding the total field $A(t) = A_q(t + \Delta t) + A_d(t)$ (see Figs. 1 and 9). In frequency space, this results in a phase shift,

$$A(\omega) = e^{i\omega\Delta t} A_q(\omega) + A_d(\omega)$$
$$= \sum_{\alpha=q,d} e^{i\delta_{\alpha,q}\omega\Delta t} A_\alpha(\omega), \tag{5}$$

where we have introduced the notation $\delta_{\alpha,q} = 1$ for $\alpha = q$ and zero for $\alpha = d$.

In a nonlinear THz experiment, the current $j(t)$ is electro-optically sampled as a function of t and Fourier transformed numerically to obtain $j(\omega)$. Multiple such traces are recorded for varied Δt to assemble the 2D spectrum $j(\omega; \Delta t)$. Inserting Eq. (5) into Eq. (3), we obtain

$$j(\omega; \Delta t) = \int \prod_{i=1}^{3} d\omega_i \, \delta\left(\omega - \sum_i \omega_i\right)$$
$$\times \sum_{\alpha_1,\alpha_2,\alpha_3=q,d} \exp\left(i\Delta t \sum_{i=1}^{3} \delta_{\alpha_i,q}\omega_i\right)$$
$$\times A_{\alpha_1}(\omega_1)\chi_{\rho\rho}(\omega_2 + \omega_3)A_{\alpha_2}(\omega_2)A_{\alpha_3}(\omega_3), \tag{6}$$

where we are summing over all combinations $\{\alpha_i\}$ of quench and drive pulse, A_q and A_d, respectively. We perform a Fourier

transform in the parametric time delay Δt to obtain

$$j(\omega; \omega_{\Delta t}) = \int \prod_{i=1}^{3} d\omega_i \, \delta\left(\omega - \sum_i \omega_i\right)$$
$$\times \sum_{\alpha_1,\alpha_2,\alpha_3=q,d} \delta\left(\omega_{\Delta t} + \sum_{i=1}^{3} \delta_{\alpha_i,q}\omega_i\right)$$
$$\times A_{\alpha_1}(\omega_1)\chi_{\rho\rho}(\omega_2 + \omega_3)A_{\alpha_2}(\omega_2)A_{\alpha_3}(\omega_3) \tag{7}$$

We can represent the various terms in the sum over $\{\alpha_i\}$ diagrammatically as depicted in Fig. 2. Here, the current is represented by a red wiggly line, and quench and probe pulses are depicted by blue and black wiggly photon lines, respectively. The density-density susceptibility $\chi_{\rho\rho}$ is represented by a fermionic bubble whose internal frequency we have labeled ω_n.

All external photon lines carry frequencies with profiles determined by the experimental bandwidth of the pulses $A_{\alpha_i}(\omega_i)$, where the directionality is marked by arrows of the photon lines. The drive pulse will constrain the external frequencies to $\sim \pm\omega_d$. In fact, we will be assuming a sufficiently narrowband drive pulse, $\tau_d \gg 1/\Delta$, such that we can approximate

$$A_d(\omega_i) \sim \delta(\omega_i - \omega_d) + \delta(\omega_i + \omega_d). \tag{8}$$

The key advantage of the pump-probe geometry lies in the appearance of the second δ function in Eq. (7) that introduces the experimentally accessible variable $\omega_{\Delta t}$. We can see this as follows. When $\alpha_1 = d$ and $\alpha_2 = \alpha_3 = q$, the δ function presents the constraint $\delta(\omega_{\Delta t} + \omega_2 + \omega_3)$ and the density-density correlation function is evaluated at $\chi(\omega_2 + \omega_3) = \chi(-\omega_{\Delta t})$. Thus, χ can be pulled out of the integral in Eq. (7) and the measured current is directly proportional to the $\chi_{\rho\rho}$-response, whose frequency dependence can be mapped out by sweeping $\omega_{\Delta t}$. The diagrammatic representation of this process is shown in Fig. 2(a). Making use of approximation (8), it follows from energy conservation that the current is nonzero only along the lines $\omega = \pm\omega_d - \omega_{\Delta t}$ in 2D frequency space $(\omega, \omega_{\Delta t})$, where j is given by

$$j(\pm\omega_d - \omega_{\Delta t}, \omega_{\Delta t}) \propto \chi_{\rho\rho}(-\omega_{\Delta t}). \tag{9}$$

As similar discussion applies to the process depicted in Fig. 2(b). Here, $\alpha_1 = \alpha_3 = d$ and $\alpha_2 = q$. The susceptibility is evaluated as $\chi(\pm\omega_d - \omega_{\Delta t})$ and determined the current along the lines $\omega = \pm 2\omega_d - \omega_{\Delta t}$ and $\omega = -\omega_{\Delta t}$. Explicitly, the current is

$$j(\pm 2\omega_d - \omega_{\Delta t}, \omega_{\Delta t}) \propto \chi_{\rho\rho}(\pm\omega_d - \omega_{\Delta t}),$$
$$j(-\omega_{\Delta t}, \omega_{\Delta t}) \propto \chi_{\rho\rho}(\omega_d - \omega_{\Delta t}) + \chi_{\rho\rho}(-\omega_d - \omega_{\Delta t}). \tag{10}$$

Figure 2(c) describes the usual THG process that is independent of the quench. In 2D Fourier space it yields a signal at $\omega_{\Delta t} = 0$ at the first and third harmonic frequencies of the drive, $\omega = \pm\omega_d, \pm 3\omega_d$, where the density-density susceptibility is evaluated at fixed values $0, \pm 2\omega_d$.

The remaining diagrams of Fig. 2 can be separated into two classes. In Fig. 2(d) $\chi_{\rho\rho}$ only depends on ω_d and the discussion of the THG case applies. In Figs. 2(e) and 2(f) the dependence of $\chi_{\rho\rho}$ on integration variables ω_i cannot be removed. As a consequence, the resonance structure of $\chi_{\rho\rho}$ is
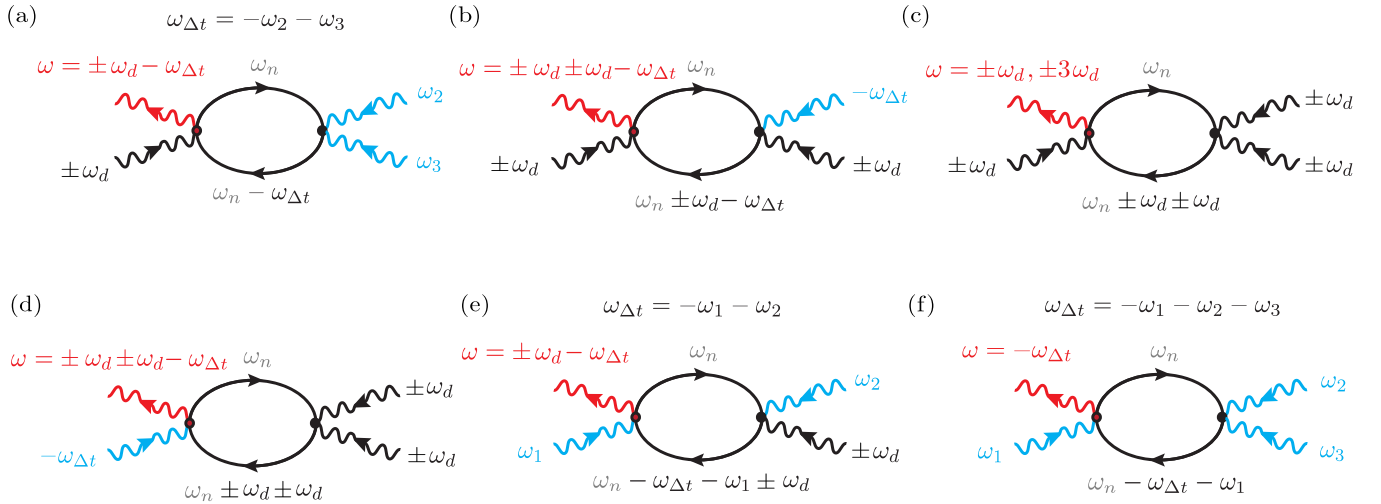
FIG. 2. Diagrammatic representation of the nonlinear processes. The wiggly lines represent photons: the black ones correspond from the driving field A_d, the blue lines correspond to the quench pulse A_q, and the red line represents the generated current. Solid lines denote fermionic bubbles that represent the nonlinear susceptibility $\chi_{\rho\rho}$. Due to the δ-function constraint in Eq. (7), all blue quench frequencies have to add up to $-\omega_{\Delta t}$. Energy conservation demands that all incoming frequencies add up to the frequency ω of the induced current.

washed out by integration and one obtains a mostly constant signal for frequencies much smaller than the bandwidth of the quench pulse.

In summary, we have shown that the signal $j(\omega, \omega_{\Delta t})$ falls onto diagonal lines $\omega = \pm n\omega_d - \omega_{\Delta t}$ with $n \in \{0, 1, 2\}$ in 2D Fourier space. From the 2D spectra, one can extract the density-density response according to

$$j(\pm 2m\,\omega_d - \omega_{\Delta t}, \omega_{\Delta t}) \propto \chi_{\rho\rho}(\pm\omega_d - \omega_{\Delta t})$$
$$+ c_1, \quad j(\pm\omega_d - \omega_{\Delta t}, \omega_{\Delta t}) \propto \chi_{\rho\rho}(-\omega_{\Delta t}) + c_2, \quad (11)$$

where $m = \{0, 1\}$ and the c_i denote the background signal that is mostly constant in the limit of a broadband quench pulse.

III. MICROSCOPICAL DESCRIPTION

Having discussed the phenomenological structure of the nonlinear response in a quench-drive experiment, let us now microscopically investigate the response current of a conventional clean superconductor subject to quench and drive pulses. The solution is obtained solving the Bloch equations derived from the pseudospin model of the BCS Hamiltonian.

A. Equations of motion with quench-drive pulses

We write the BCS Hamiltonian using the pseudospin formalism [3,7,38,39] as

$$\hat{H} = \sum_{\mathbf{k}} \mathbf{b}_{\mathbf{k}} \cdot \hat{\sigma}_{\mathbf{k}}, \quad (12)$$

with the pseudospin vector

$$\hat{\sigma}_{\mathbf{k}} = \tfrac{1}{2} \hat{\Psi}_{\mathbf{k}}^{\dagger} \tau \hat{\Psi}_{\mathbf{k}}, \quad (13)$$

which is defined in Nambu-Gor'kov space, with spinor $\hat{\Psi}_{\mathbf{k}} = (\hat{c}_{\mathbf{k},\uparrow}^{\dagger} \quad \hat{c}_{-\mathbf{k},\downarrow})$ and the Pauli matrices $\tau = (\tau_1, \tau_2, \tau_3)$. The pseudomagnetic field is defined by the vector

$$\mathbf{b}_{\mathbf{k}} = (-\Delta' f_{\mathbf{k}}, -\Delta'' f_{\mathbf{k}}, \varepsilon_{\mathbf{k}}), \quad (14)$$

where $\varepsilon_{\mathbf{k}} = \xi_{\mathbf{k}} - \mu$, $\xi_{\mathbf{k}}$ being the fermionic band dispersion, μ the chemical potential. The superconducting order parameter $\Delta_{\mathbf{k}} = \Delta f_{\mathbf{k}} = (\Delta' + i\Delta'') f_{\mathbf{k}}$ satisfies the gap equation

$$\Delta_{\mathbf{k}} = \Delta f_{\mathbf{k}} = V f_{\mathbf{k}} \sum_{\mathbf{k}'} f_{\mathbf{k}'} \langle \hat{c}_{-\mathbf{k}',\downarrow} \hat{c}_{\mathbf{k}',\uparrow} \rangle. \quad (15)$$

Here, V is the pairing strength, and $f_{\mathbf{k}}$ the form factor of the superconducting order parameter. For s-wave pairing one has $f_{\mathbf{k}} = 1$.

In the presence of an external field represented by the vector potential $\mathbf{A}(t)$, the pseudospin changes in time according to

$$\sigma_{\mathbf{k}}(t) = \sigma_{\mathbf{k}}(0) + \delta\sigma_{\mathbf{k}}(t), \quad (16)$$

with $\sigma_{\mathbf{k}} = \langle \hat{\sigma}_{\mathbf{k}} \rangle$ and $\delta\sigma_{\mathbf{k}}(t) = (x_{\mathbf{k}}(t), y_{\mathbf{k}}(t), z_{\mathbf{k}}(t))$. The external electromagnetic field is included in the pseudomagnetic field by means of the minimal substitution $\mathbf{k} \rightarrow \mathbf{k} - e\mathbf{A}(t)$ in the fermionic energy, resulting in

$$\mathbf{b}_{\mathbf{k}}(t) = (-\Delta'(t) f_{\mathbf{k}}, -\Delta''(t) f_{\mathbf{k}}, (\varepsilon_{\mathbf{k}-e\mathbf{A}(t)} + \varepsilon_{\mathbf{k}+e\mathbf{A}(t)})/2). \quad (17)$$

The Heisenberg equation of motion for the pseudospin can be written in Bloch form, $\partial_t \sigma_{\mathbf{k}} = 2\mathbf{b}_{\mathbf{k}} \times \sigma_{\mathbf{k}}$, providing the set of differential equations

$$\partial_t x(t) = -(\varepsilon_{\mathbf{k}-e\mathbf{A}} + \varepsilon_{\mathbf{k}+e\mathbf{A}}) y(t) - \frac{f_{\mathbf{k}}}{E_{\mathbf{k}}} \varepsilon_{\mathbf{k}} \delta\Delta''(t)$$
$$+ 2\delta\Delta''(t) f_{\mathbf{k}} z(t),$$

$$\partial_t y(t) = 2\varepsilon_{\mathbf{k}} x(t) + 2[\Delta + \delta\Delta'(t)] f_{\mathbf{k}} z(t) \quad (18)$$
$$- \delta\Delta'(t) f_{\mathbf{k}} \frac{\varepsilon_{\mathbf{k}}}{E_{\mathbf{k}}} + \frac{\Delta f_{\mathbf{k}}}{2E_{\mathbf{k}}} (\varepsilon_{\mathbf{k}-e\mathbf{A}} + \varepsilon_{\mathbf{k}+e\mathbf{A}} - 2\varepsilon_{\mathbf{k}}),$$

$$\partial_t z(t) = -2\,\Delta f_{\mathbf{k}}\, y(t) - \frac{\Delta f_{\mathbf{k}}^2}{E_{\mathbf{k}}} \delta\Delta''(t) - 2\delta\Delta''(t) f_{\mathbf{k}} x(t),$$

where $\delta\Delta(t) = \delta\Delta'(t) + i\,\delta\Delta''(t)$ is the time-dependent variation of the order parameter induced by the external field, such that $\Delta(t) = \Delta + \delta\Delta(t)$. Here, we assumed a real order parameter at the initial time $t = 0$, so that $y(0) = 0$. The solution of Eq. (18) provides the time-dependent evolution of pseudospins, from which the time-dependent order parameter $\Delta(t)$ and the generated current $j(t)$ can be calculated. A detailed derivation of the equations of motion is given in Appendix A.

B. Nonlinear current

The current generated by the superconductor in this quench-drive setup is given by the general expression

$$\mathbf{j}(t, \Delta t) = e \sum_{\mathbf{k}} \mathbf{v}_{\mathbf{k}-e\mathbf{A}(t,\Delta t)} \langle \hat{n}_{\mathbf{k}}(t, \Delta t) \rangle, \qquad (19)$$

where the velocity is calculated as $\mathbf{v}_{\mathbf{k}-e\mathbf{A}(t,\Delta t)} = \nabla_{\mathbf{k}}\varepsilon_{\mathbf{k}-e\mathbf{A}(t,\Delta t)}$, and the charge density is defined as $\langle \hat{n}_{\mathbf{k}}(t, \Delta t) \rangle = \langle \hat{c}_{\mathbf{k},\uparrow}^{\dagger}\hat{c}_{\mathbf{k},\uparrow} + \hat{c}_{\mathbf{k},\downarrow}^{\dagger}\hat{c}_{\mathbf{k},\downarrow}\rangle(t, \Delta t)$. We can expand the velocity as a function of the vector potential $\mathbf{A}(t, \Delta t)$, and expand the current in powers of the external field. The first nonvanishing term of the nonlinear current $j^{NL}(t, \Delta t)$ generated by the driving pulse is the third-order component

$$\mathbf{j}^{(3)}(t, \Delta t) = -2e^2 \sum_{\mathbf{k}} \sum_{i=x,y} \mathbf{A}(t, \Delta t) \cdot \mathbf{r}_i\, \partial_{k_i}\mathbf{v}_{\mathbf{k}}\, z_{\mathbf{k}}(t, \Delta t),$$

$$(20)$$

where $z_{\mathbf{k}}(t, \Delta t)$ is the third component of the pseudospin vector $\sigma_{\mathbf{k}}(t, \Delta t)$, that contains the information of the state of the system perturbed by the quench pulse. The unit vector $\mathbf{r}_i$, $i = x, y$, represents the two directions along which the output current is measured.

IV. NUMERICAL RESULTS

We now present the results obtained from the numerical implementation of time-dependent Bloch equations described in the previous section, solved by means of a Runge-Kutta-4 algorithm without linearization or further analytical approximations. We used the fermionic band dispersion $\varepsilon_{\mathbf{k}} = -2t(\cos k_x + \cos k_y)$ at half filling, setting the lattice constant $a = 1$. The point $\mu = 0$ is special in the sense that it has perfect particle-hole symmetry as well as a van Hove singularity at the Fermi level. But from the viewpoint of collective modes, this symmetry point does not bear any special significance other than presenting a local minimum of the Higgs contribution compared to single-particle excitations in the nonlinear response [15].

We used the values of $t = 125$ meV for the nearest-neighbor hopping energy, s-wave order parameter $\Delta_0 = 15.8$ meV (corresponding to a frequency of 3.82 THz), and a summation over the full Brillouin zone with a square sampling and a total number of $N_{\mathbf{k}} = 10^6$ points. For the time-dependent evolution we used a time step of $\delta t = 3 \times 10^{-4}$ ps, and for the quench-drive delay $\delta\Delta t = 2.5 \times 10^{-2}$ ps. For the quench we used a few-cycles pulse with central frequency $\omega_q = 4.77$ THz, while for the driving we used an asymmetric pulse with central frequency $\omega_d = 4.3$ THz, so that both sat-
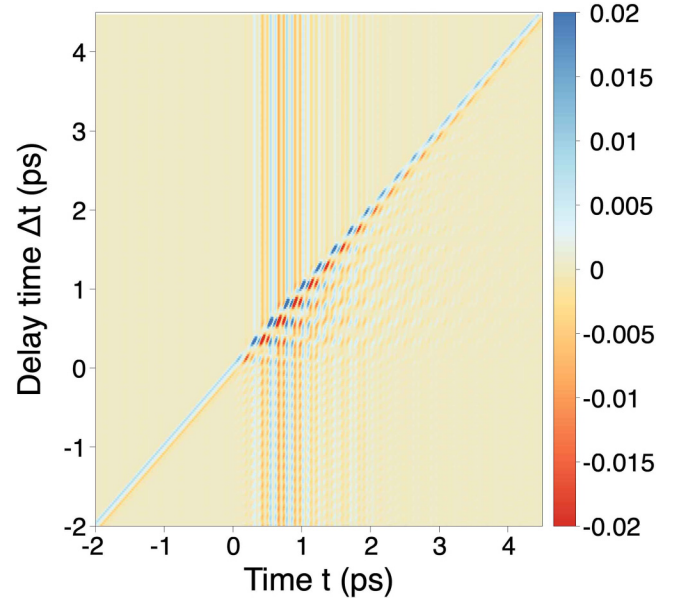

FIG. 3. Time-delay two-dimensional plot of the generated nonlinear current. 2D plot of the nonlinear output current $j^{NL}(t, \Delta t)$ generated by the driven superconductor, as a function of real time t and the quench-drive delay time Δt. The narrow diagonal stripes are generated by the quench, while the vertical ones are the response to the drive pulse. The intersection provides a wave mixing pattern for $t, \Delta t \in [0, 2]$ ps. Here we used the asymmetric drive pulse, with quench and drive pulse frequencies respectively $\omega_q = 4.77$ THz and $\omega_d = 4.3$ THz.

isfy the condition $\omega_{q(d)} < 2\Delta$. Both pulses were considered linearly polarized along the $\mathbf{x}$ direction, while the maximum amplitudes of the electric field of quench and drive pulses were $E_q = 10.5$ kV/cm and $E_d = 4.7$ kV/cm, respectively, assuming a value for the lattice constant of $a = 3$ Å. For more details on the pulses used, see Appendix B. In Appendix C we analyze the 2D spectra for the case of cross polarization of the two pulses, while in Appendix D we show additional results that were computed using a symmetric Gaussian driving pulse instead of an asymmetric one.

A. Two-dimensional quench-drive spectroscopy

We solved the time-dependent equation of motion in the quench-drive spectroscopy setup using the pseudospin model, and calculated the nonlinear current generated by the condensate as described in the previous section. The result plotted as a function of the real time evolution t and the quench-drive delay time Δt, which is measured as the interval between the maximal peaks of the envelopes of the two pulses (see Appendix B for more details on the pulse shapes), is shown in Fig. 3. We notice that the diagonal line signifies the arrival of the quench pulse, which overlaps with the drive for times $t = \Delta t$ in the range $t, \Delta t \in [0, 2]$ ps. In this region the response is modulated as a function of the delay time Δt.

Next, we Fourier transform the real time variable t into the frequency ω. In Fig. 4 we show the nonlinear generated current intensity as a function of the quench-drive delay time Δt, namely $|j^{NL}(\omega, \Delta t)|$. We notice that both the first and
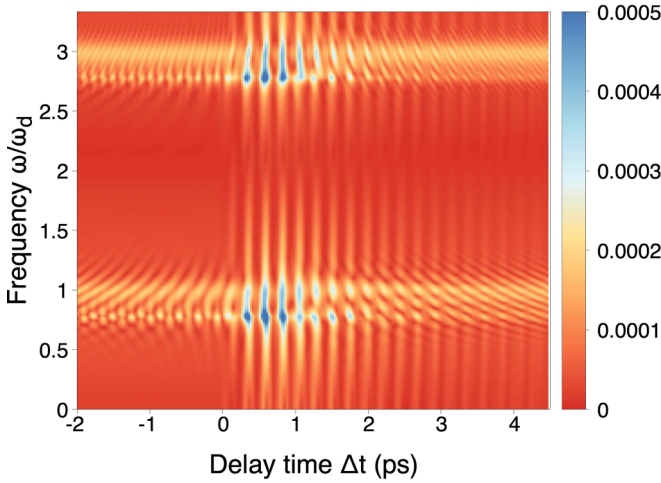
FIG. 4. Frequency-time delay two-dimensional plot of the generated nonlinear current. 2D plot of the nonlinear current $j^{NL}(\omega, \Delta t)$ generated by the driven superconductor, as a function of relative frequency ω/ω_d (with driving frequency $\omega_d = 4.3$ THz) and the quench-drive delay time Δt. This corresponds to a Fourier transform in the horizontal direction in Fig. 3. The fundamental ($\omega = \omega_d = 4.3$ THz) and third ($\omega = 3\omega_d = 12.9$ THz) harmonics are both modulated in the delay time Δt.

third harmonics of the fundamental driving frequency ω_d are modulated in delay time Δt, with maximum intensity in the interval 0 ps $\leqslant \Delta t \leqslant$ 2 ps, which corresponds to the range of interference between the quench and the drive pulses, as shown in Fig. 3. Additionally, the signal intensity does not vanish away from ω_d and $3\omega_d$, where we instead observe a striped pattern, with each intensity line tilted towards the central time $\Delta t = 1$ ps.

These features can be more readily interpreted by plotting the 2D Fourier transform of the current, i.e., as a function of the frequency ω and the delay-time frequency $\omega_{\Delta t}$, respectively, shown in Fig. 5. In particular, we notice the first and
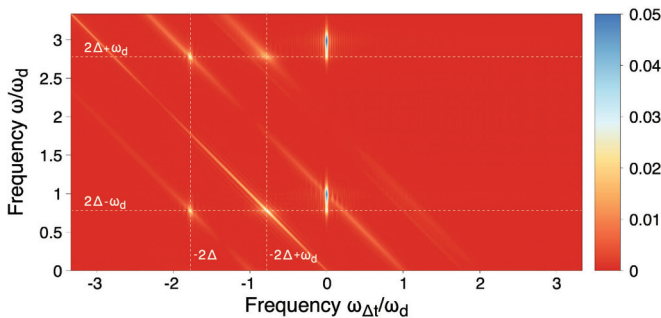

FIG. 5. Two-dimensional Fourier-transformed plot of the nonlinear current. 2D plot of the generated nonlinear output current intensity $j^{NL}(\omega, \omega_{\Delta t})$ as a function of the real frequency ω and the quench-drive delay frequency $\omega_{\Delta t}$. It corresponds to the two-dimensional Fourier transform of the data in Fig. 3. The vertical response at $\omega_{\Delta t} = 0$ corresponds to the quench-free superconducting signal, namely the high-harmonic generation due to the driving field. The diagonal lines, instead, represent the transient modulation of the higher harmonics due to the quench-drive wave mixing.
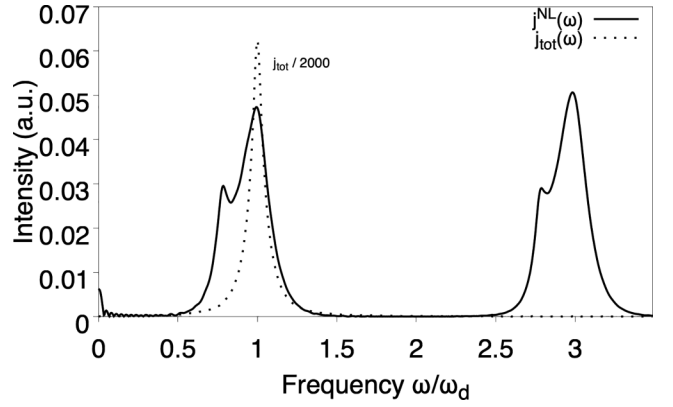

FIG. 6. Driven high-harmonic generation. Plot of the generated nonlinear (continuous line) and total (dashed line) current as a function of frequency, $j^{NL}(\omega)$ and $j_{tot}(\omega)$, respectively. This plot corresponds to a vertical cut in Fig. 5 along ω for $\omega_{\Delta t} = 0$. The peaks at $\omega = \omega_d = 4.3$ THz and $\omega = 3\omega_d = 12.9$ THz correspond to the fundamental and third harmonics, respectively. The smaller peak at $\omega = 12$ THz corresponds to the transient excitation of Higgs and quasiparticles with $\omega = \omega_d + 2\Delta$, due to the asymmetric driving pulse.

third harmonics as strong peaks in the central vertical line, at $\omega_{\Delta t} = 0$, which corresponds to the equilibrium response of the driving pulse in the absence of the quench. Note that it is sufficient to plot two quadrants of the nonlinear current in 2D frequency space, since it follows from $j(t, \Delta t) \in \mathbb{R}$ that $j(\omega, \omega_{\Delta t}) = j(-\omega, -\omega_{\Delta t})$.

The modulations in Δt appear here as broad diagonal lines in 2D frequency space as expected from Eq. (11). These features correspond to a dynamically generated four-wave mixing signal due to both the quench and the drive pulses.

B. High-harmonic generation and transient excitation of the superconductor

To clearly distinguish the shape and position of the peaks observed in the frequency 2D plot, we performed one-dimensional cuts of Fig. 5 along various lines. Fig. 6 shows the plot along the vertical line at $\omega_{\Delta t} = 0$. This corresponds to an equilibrium high-harmonic generation due to the driving pulse only. We observe a first harmonic peak at ω_d and a third harmonic signal at $3\omega_d$. Measurement of the temperature dependence of the THG peak would correspond to a usual THz THG experiment. The intensities of the fundamental and third harmonics (continuous line) are of the same order, since only the third order is plotted. The total current has a dominant linear first harmonic response (dashed line). In addition to the first and third harmonics, however, we notice the presence of an additional shoulder peaks at a frequency $\omega = 2\Delta + \omega_d$ and at $\omega = 2\Delta - \omega_d$. These are the result of the intrinsic Higgs and quasiparticle resonance at 2Δ [40] in conjunction with a wave-mixing process with a driving photon of frequency $\pm\omega_d$.

In Fig. 7 we show the prototypical case of a horizontal cut in Fig. 5 along $\omega = 3\omega_d$. The peak at $\omega_{\Delta t}/\omega_d = 0$ is the equilibrium third harmonic, visible in Fig. 6, while the smaller
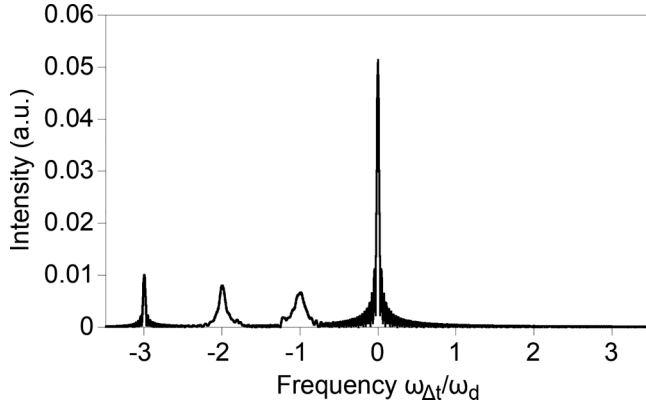
FIG. 7. Transient modulation of higher harmonics. Frequency-resolved spectral weight of the third harmonic current as a function of $\omega_{\Delta t}$, $j^{NL}(\omega_{\Delta t}, \omega = 3\omega_d)$. This corresponds to a horizontal cut in the 2D Fourier-transform plot in Fig. 5 along $\omega_{\Delta t}$ at $\omega = 3\,\omega_d$. It is possible to identify a transient modulation at frequencies $-\omega_d$, $-2\omega_d$, and $-3\omega_d$.

peaks at $\omega_{\Delta t}/\omega_d = -1, -2, -3$ stem from the modulation of the third harmonic due to the quench. Additional smaller peaks appear in Fig. 4 as a modulation in the delay time Δt of the third harmonic, giving rise to the characteristic striped pattern.

Figure 8 corresponds to a diagonal line in the 2D plot of Fig. 5 passing through the point $\omega_{\Delta t} = 0$, $\omega = \omega_d$, and projected along the $\omega_{\Delta t}$ axis. The peak at $\omega_{\Delta t} = 0$ is the signal of the first harmonic. Of particular interest is the peak at $\omega_D = -2\Delta$, which is a direct consequence of the quasiparticle resonance at $\pm 2\Delta$, represented by the process in Fig. 2(d). Due to the wave mixing of the quench and the drive, we have here isolated the intrinsic superconducting response with the characteristic frequency of 2Δ.

Moreover, the peaks in Fig. 5 along the diagonals placed at $\omega_{\Delta t} = -2\Delta + \omega_d$ are resulting from the process represented by the diagram in Fig. 2(b), and they disappear when quench and drive have perpendicular polarization,
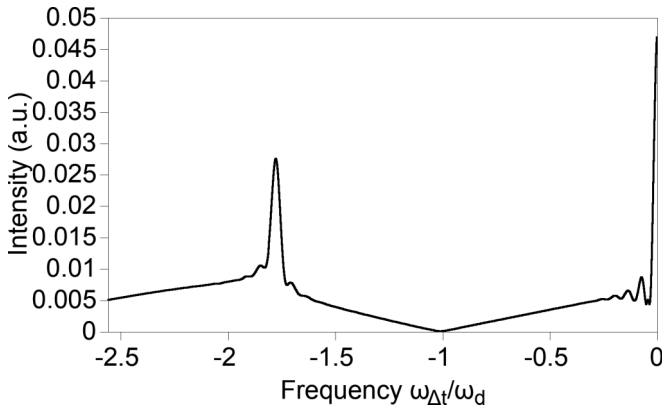

FIG. 8. Transient excitation. This plots corresponds to a diagonal cut in the 2D Fourier-transform plot in Fig. 5 along the line $\omega = -\omega_{\Delta t} + \omega_d$. It is possible to identify a peak at a frequency $\omega_{\Delta t} = -7.7$ THz $= -1.8\omega_d = -2\Delta_0$.

since the corresponding interaction vertex vanishes (see Appendix C).

V. DISCUSSION

We can understand all features in the spectrum shown in Fig. 5 by considering each of the diagrams in Fig. 2 that represent the induced current expanded to third order in various combinations of powers of A_d and A_q. The equilibrium THG signal proportional to A_d^3 has to be independent of Δt and therefore falls onto the vertical line $\omega_{\Delta t} = 0$ in the 2D spectrum $j(\omega, \omega_{\Delta t})$. This is represented by the diagram Fig. 2(c), where only the driving field acts on the condensate, and the current spectrum can be described as a function of real-time evolution as in Fig. 6. Interestingly, we also notice that, in addition to the aforementioned fundamental and third harmonics, a shoulder peak of the third harmonic at a frequency $\omega_d + 2\Delta$ appears when the driving pulse is asymmetric and not Gaussian shaped (see Appendix D for the data with the symmetric envelope). This is the direct consequence of the effective quench induced by the driving, which launches free Higgs oscillations alongside the quasiparticle contribution and enhances the intensity of the nonlinear susceptibility at $\omega_H = 2\Delta$ [3,7,36]. In principle, a THG experiment for a single temperature would suffice to identify the collective mode resonance. However, this approach strictly relies on the condition $2\Delta \approx 2\omega_d$ and is specific to the asymmetric pulse shape [36] (see also Appendix D).

The processes described by diagrams (a), (b), and (d)–(f) in Fig. 2, which involve at least one photon of the quench, are responsible for the signals along diagonal lines $\omega = \pm n\omega_d - \omega_{\Delta t}$ with $n \in \{0, \pm 1, \pm 2\}$. The spectral window in which these lines can be observed are related to the bandwidth of the quench pulse. Here, we differentiate between even and odd n. Odd diagonal lines show a peak at $\omega_{\Delta t} = -2\Delta$ and even diagonals are peaked at $\omega_{\Delta t} = \omega_d - 2\Delta$. This is expected from Eq. (11) since the susceptibility $\chi_{\rho\rho}$ is peaked at 2Δ for the modeled single-band superconductor. From Eq. (11), we would additionally expect a peak at $\omega_{\Delta t} = -\omega_d - 2\Delta$ for the line at $n = -2$. However, while the diagonal $n = -2$ line in principle is present, its spectral weight is negligibly small within the corresponding frequency range. Note that diagonal lines at $\pm n$ are related by frequency inversion $j(\omega, \omega_{\Delta t}) = j(-\omega, -\omega_{\Delta t})$.

By inspecting the 2D spectrum in Fig. 5, it is now straightforward to extract the resonances of the nonlinear susceptibility $\chi_{\rho\rho}$. In our case, we observe the four peaks on the diagonal lines from which we extract the value 2Δ. If the superconducting condensate supports additional collective modes that nonlinearly couple in the electromagnetic response, their mode frequencies can be readily extracted as well.

VI. CONCLUSION AND OUTLOOK

In this work we proposed and analyzed a pump-probe spectroscopy setup on conventional clean superconductors with a combination of a single-cylce THz quench pulse and a multicycle driving THz probe field. We used a numerical approach based on the Anderson-pseudospin model to solve
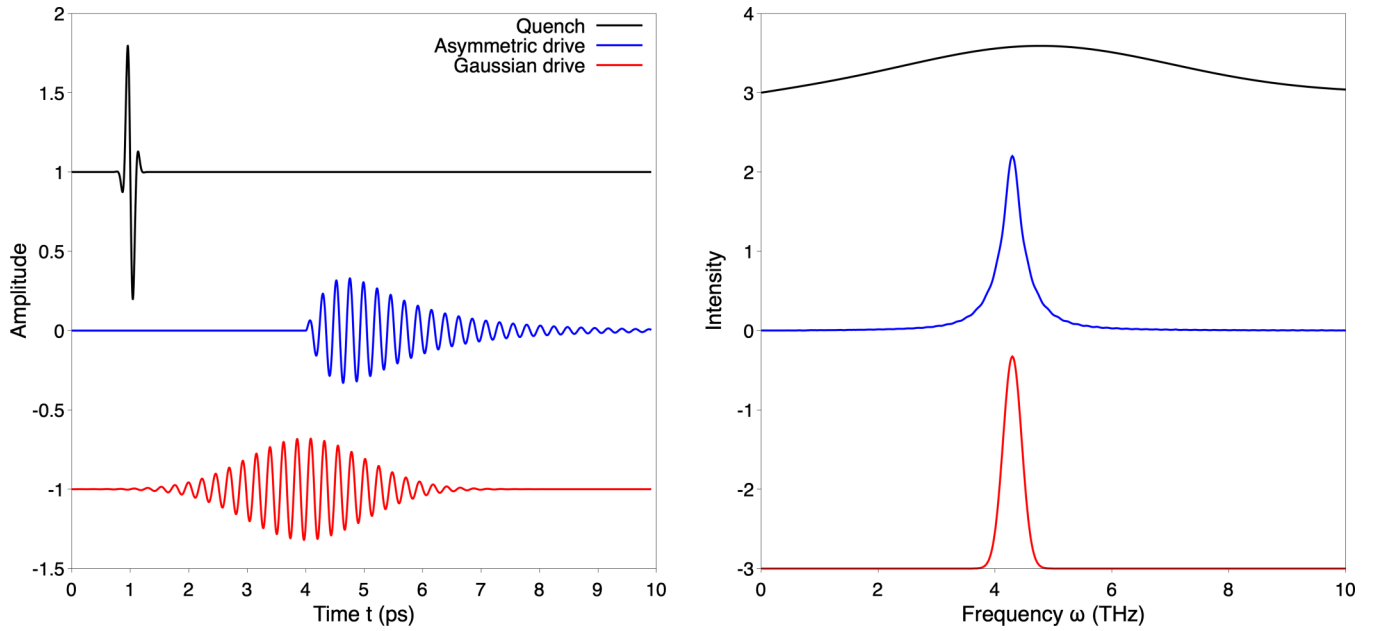
FIG. 9. Quench and drive pulses. Plot of the amplitude of the vector potential A corresponding to the quench (top left, frequency $\omega_q = 4.77$ THz) and drive pulses used in the calculations: the asymmetric drive pulse (center left) and Gaussian shaped drive pulse (bottom left) have a frequency $\omega_d = 4.3$ THz. On the right their Fourier spectrum in frequency is shown: the asymmetric drive has a sharp peak in frequency with a slower decay, while the Gaussian-shaped drive is narrower in frequency.

the equations of motion and to calculate the generated nonlinear current. In addition, we investigated the nonlinear optical processes by means of a diagrammatic approach to interpret and explain the obtained results.

In particular, we showed that, in addition to the usual third harmonic generation measured in driving experiments, additional features are obtained in a two-dimensional spectrum of the nonlinear generated current. These features are manifest as diagonal lines in 2D frequency space of the time and pump-probe delay and allow for a direct extraction of resonances in the nonlinear susceptibility. The susceptibility encodes the intrinsic superconducting response of the quasiparticles and resonances of transient excitation of the Higgs mode.

The advantage of a two-dimensional analysis of quench-drive spectroscopy is manifest in the possibility of scanning a wider frequency spectrum at one time, with fixed parameters of quench and drive pulses, by scanning the quench-drive delay time. In addition, with the present setup the quench pulse allows one to push the system out of equilibrium, quenching and shrinking the superconducting gap, allowing the driving pulse to probe different states of the superconductor, resulting in different peak profiles and positions in the 2D frequency spectra.

It is also interesting to examine the possibility of extending the quench-drive spectroscopy framework to the case of cuprates, which exhibit a different symmetry of the order parameter in momentum space, and preformed phase-incoherent Cooper pairs [41], which can reveal more information on the competing orders and their symmetries.

All in all, we believe that this work can pave the way towards coherent time-dependent multidimensional spectroscopy on superconductors in the THz regime. A full two-dimensional pump-pump-probe spectroscopy with coherent pulses will be the focus of a future work. Its

possibilities range from coherent control of superconductors to the study of competing orders, such as superconductivity, charge-density wave, and biplasmon among others [21,42]. Other systems where the Higgs response is known to be
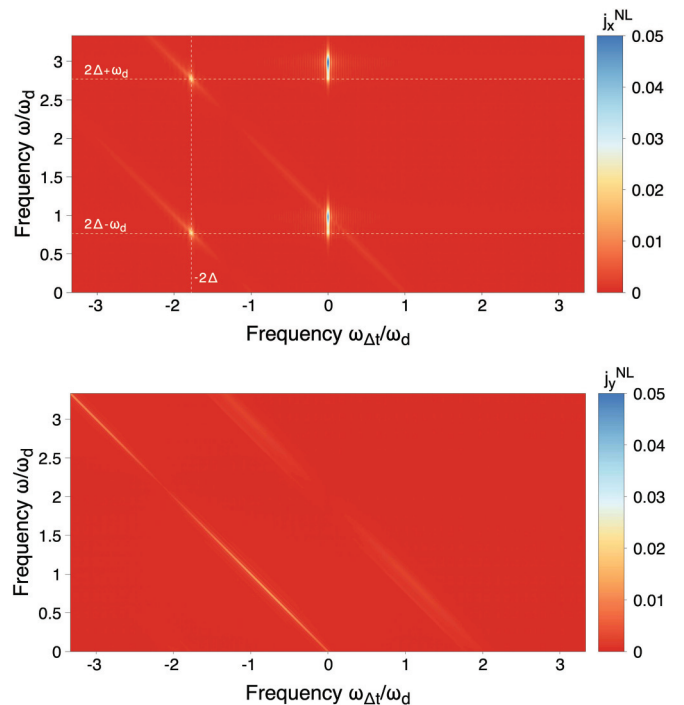

FIG. 10. Nonlinear current spectra for cross-polarized pulses. 2D Fourier transform of x (top) and y components (bottom) of the nonlinear current response for cross-polarized quench (linearly polarized along the x axis) and drive (linearly polarized along the y axis).
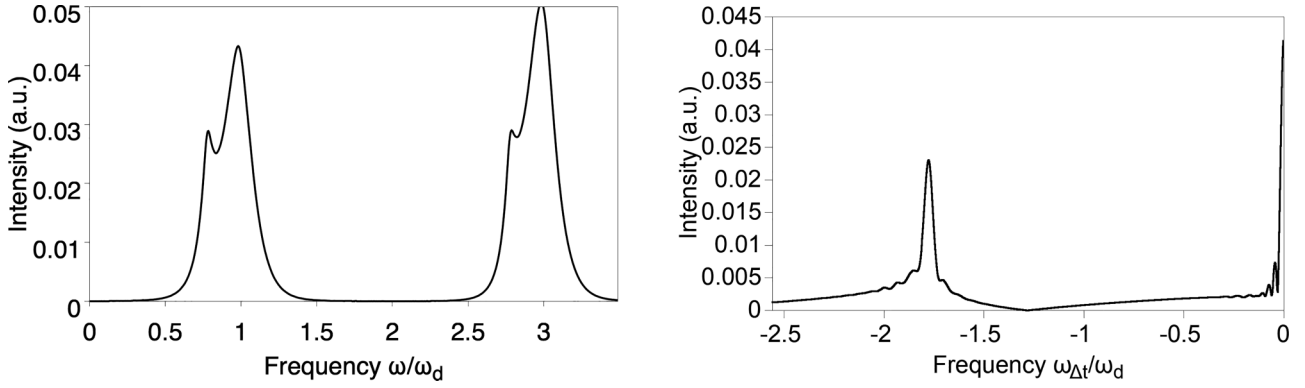
FIG. 11. Nonlinear current along the x axis: traces from the 2D Fourier transform. Left: Nonlinear current as a function of the frequency ω, obtained with a trace along the vertical axis from the left plot in Fig. 10. Right: Nonlinear current as a function of $\omega_{\Delta t}$ with the constraint $\omega = \omega_d - \omega_{\Delta t}$, obtained from a diagonal cut passing by the fundamental harmonic of the left plot in Fig. 10.

enhanced, such as cuprates, could be interesting to investigate with this spectroscopic approach, to efficiently study the transient nonequilibrium response of quasiparticles and the Higgs mode and to unveil the features of their rich phase diagram.

ACKNOWLEDGMENTS

APPENDIX A: PSEUDOSPIN MODEL

In this Appendix we will derive the equations of motion for the order parameter within the pseudospin formalism. We note that all results shown in the paper are computed within a
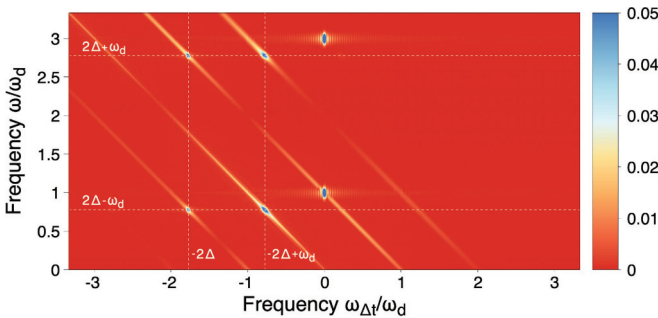

FIG. 12. Two-dimensional Fourier-transformed plot of the nonlinear current. 2D plot of the generated nonlinear output current intensity $j^{NL}(\omega, \omega_{\Delta t})$ as a function of the real frequency ω and the quench-drive delay frequency $\omega_{\Delta t}$. It corresponds to the two-dimensional Fourier transform of the data in Fig. 3. The vertical response at $\omega_{\Delta t} = 0$ corresponds to the quench-free superconducting signal, namely the high-harmonic generation due to the driving field. The diagonal lines, instead, represent the transient modulation of the higher-harmonics due to the quench-drive wave mixing. The symmetric Gaussian shaped driving pulse was used here.

fully numerical approach that does not rely on any numerical approximation.

We first write the BCS Hamiltonian using the pseudospin formalism as

$$\hat{H} = \sum_{\mathbf{k}} \mathbf{b}_{\mathbf{k}} \hat{\sigma}_{\mathbf{k}}, \tag{A1}$$

with the pseudospin

$$\hat{\sigma}_{\mathbf{k}} = \tfrac{1}{2} \hat{\Psi}_{\mathbf{k}}^{\dagger} \tau \hat{\Psi}_{\mathbf{k}}, \tag{A2}$$

$\tau = (\tau_1, \tau_2, \tau_3)$ being the vector of the Pauli matrices $\tau_{i=1,2,3}$, and the pseudomagnetic field

$$\mathbf{b}_{\mathbf{k}} = (-\Delta' f_{\mathbf{k}}, -\Delta'' f_{\mathbf{k}}, \varepsilon_{\mathbf{k}}), \tag{A3}$$

using the gap equation

$$\Delta_{\mathbf{k}} = \Delta f_{\mathbf{k}} = V f_{\mathbf{k}} \sum_{\mathbf{k}'} f_{\mathbf{k}'} \langle \hat{c}_{-\mathbf{k}',\downarrow} \hat{c}_{\mathbf{k}',\uparrow} \rangle. \tag{A4}$$

Here $\hat{c}$ is the electronic annihilation operator, $f_{\mathbf{k}}$ is the superconducting form factor, $\varepsilon_{\mathbf{k}}$ is the electronic band dispersion. In the presence of an external field represented by the vector potential $\mathbf{A}(t)$, we get

$$\sigma_{\mathbf{k}}(t) = \sigma_{\mathbf{k}}(0) + \delta\sigma_{\mathbf{k}}(t), \tag{A5}$$

with $\delta\sigma_{\mathbf{k}}(t) = (x_{\mathbf{k}}(t), y_{\mathbf{k}}(t), z_{\mathbf{k}}(t))$, and

$$\mathbf{b}_{\mathbf{k}}(t) = (-\Delta'(t) f_{\mathbf{k}}, -\Delta''(t) f_{\mathbf{k}}, \varepsilon_{\mathbf{k}-e\mathbf{A}(t)} + \varepsilon_{\mathbf{k}+e\mathbf{A}(t)}). \tag{A6}$$

The equation of motion for the pseudomagnetic field can be written in Bloch form, $\partial_t \sigma_{\mathbf{k}} = 2\mathbf{b}_{\mathbf{k}} \times \sigma_{\mathbf{k}}$. We now write the three components of the Bloch equation by applying to the time-dependent pseudospin the ansatz described above:

$$\sigma_x(t) = \sigma_x^{\text{eq}} + x(t),$$
$$\sigma_y(t) = y(t),$$
$$\sigma_z(t) = \sigma_z^{\text{eq}} + z(t), \tag{A7}$$

with $\sigma_y^{\text{eq}} = 0$ under the assumption of real order parameter, $\sigma_x^{\text{eq}} = \Delta/(2E_{\mathbf{k}})$, $\sigma_z^{\text{eq}} = -\varepsilon_{\mathbf{k}}/(2E_{\mathbf{k}})$, where the quasiparticle energy dispersion is $E_{\mathbf{k}} = \sqrt{\varepsilon_{\mathbf{k}}^2 + \Delta^2 f_{\mathbf{k}}^2}$.

Thus, the Bloch equations result in

$$\partial_t x(t) = -(\varepsilon_{\mathbf{k}-e\mathbf{A}} + \varepsilon_{\mathbf{k}+e\mathbf{A}})y(t) - \frac{f_{\mathbf{k}}}{E_{\mathbf{k}}}\varepsilon_{\mathbf{k}}\delta\Delta''(t)$$
$$+ 2\delta\Delta''(t)f_{\mathbf{k}}z(t),$$

$$\partial_t y(t) = 2\varepsilon_{\mathbf{k}}x(t) + 2(\Delta + \delta\Delta'(t))f_{\mathbf{k}}z(t) - \delta\Delta' f_{\mathbf{k}}\frac{\varepsilon_{\mathbf{k}}}{E_{\mathbf{k}}}$$
$$+ \frac{\Delta f_{\mathbf{k}}}{2E_{\mathbf{k}}}(\varepsilon_{\mathbf{k}-e\mathbf{A}} + \varepsilon_{\mathbf{k}+e\mathbf{A}} - 2\varepsilon_{\mathbf{k}}),$$

$$\partial_t z(t) = -2\,\Delta f_{\mathbf{k}}\,y(t) - \frac{\Delta f_{\mathbf{k}}^2}{E_{\mathbf{k}}}\delta\Delta''(t) - 2\delta\Delta''(t)f_{\mathbf{k}}x(t).$$
$$\text{(A8)}$$

with $\mathbf{A}(t) = \mathbf{A}_q(t) + \mathbf{A}_d(t)$, $\delta\Delta(t) = \delta\Delta'(t) + i\,\delta\Delta''(t)$ being the time-dependent variation of the order parameter induced by the external field, such that $\Delta(t) = \Delta + \delta\Delta(t)$. We introduce now the quench-drive delay time $\Delta t = t_d - t_q$, which measures the time distance of the peaks of the two pulses, and we put $t_d = 0$, so that we can rewrite $\mathbf{A}(t) = \overline{\mathbf{A}}_q(t + \Delta t) + \overline{\mathbf{A}}_d(\bar{t})$.

APPENDIX B: QUENCH AND DRIVE PULSES

As mentioned in the main text, in the quench-drive setup we adopted three different kinds of pulses: a few-cycles quench, and two different kind of drives, either asymmetric or with a Gaussian envelope profile (Fig. 9), all of them polarized in x direction (due to the symmetry of the superconductor order parameter, this assumption can be made without loss of generality).

The quench pulse is characterized by a very few cycles and its vector potential can be written as

$$A_q(t) = A_q^0\,e^{-(t-t_q)^2/\tau_q^2}\cos[\omega_q(t - t_q)], \qquad \text{(B1)}$$

with $\tau_q = 0.1$ ps and the quench central frequency $\omega_q = 4.77$ THz.

The asymmetric driving pulse is defined by the expression

$$A_d(t) = \begin{cases} A_d^0\dfrac{\sin[\omega_d(t - t_d)]}{1 + (t - t_d)^2}(t - t_d)e^{-(t-t_d)/\tau_d} & \text{for } t \geqslant t_d, \\ 0 & \text{for } t < t_d, \end{cases}$$
$$\text{(B2)}$$

with $\tau_d = 2$ ps and the driving central frequency $\omega_d = 4.3$ THz. The driving pulse reaches its maximum intensity after ≈ 1 ps, and then slowly decays within ≈ 5 ps. Therefore, the initial part of the drive acts as an effective quench on the superconductor, while the its decay drives the condensate and its collective modes.

Similarly to the quench pulse, the time-symmetric drive with Gaussian envelope is

$$A_d(t) = A_d^0 e^{-(t-t_0)^2/\tau_d^2}\cos[\omega_d(t - t_0)]. \qquad \text{(B3)}$$

APPENDIX C: CROSS POLARIZATION OF QUENCH AND DRIVE PULSES

So far, we have analyzed the setup with parallel linearly polarized quench and drive pulses along the x axis. For s-wave BCS superconductors, the direction of the polarization of the pulses is arbitrary and does not affect the results, as long as the polarization is kept parallel.
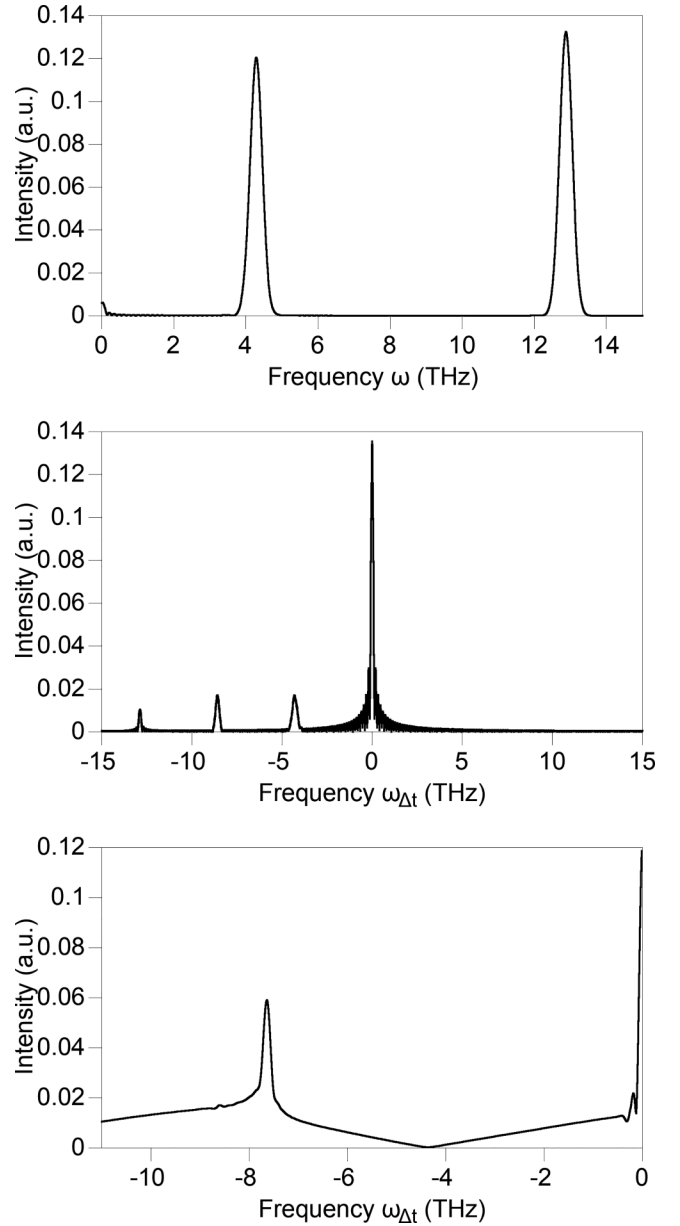

FIG. 13. High-harmonic generation and transient modulation with Gaussian drive. Top: nonlinear current $j^{NL}(\omega)$ at $\omega_{\Delta t} = 0$. In contrast to Fig. 6, no peak at $\omega = 2\Delta + \omega_d$ is present in this case. Center: nonlinear current modulation as a function of the quench-drive frequency $\omega_{\Delta t}$, $j^{NL}(\omega_{\Delta t}, \omega = 3\omega_d)$. This corresponds to Fig. 7 using the Gaussian envelope for the drive pulse. Bottom: $j^{NL}(\omega_{\Delta t})$ obtained with the condition $\omega = -\omega_{\Delta t} + \omega_d$, equivalent to Fig. 8.

In this section, we study the case of nonparallel quench and drive pulses. The drive is fixed along the x axis and the quench is linearly polarized along the y axis. We calculate the output current along the two orthogonal axes x and y. The corresponding spectra are plotted in Fig. 10 as a function of ω and $\omega_{\Delta t}$. The fundamental and third harmonic signals are still present in the Fourier transform of the current along x, together with the side peaks at $2\Delta \pm \omega_d$. Along the diagonals, the peaks at $\omega_{\Delta t} = -2\Delta_0 + \omega_d$ are absent, as shown in Fig. 11 (in contrast to the parallel polarization, as shown in Fig. 8), while the ones located at $\omega_{\Delta t} = -2\Delta_0$ are still

present. This is due to the fact that the quench and the drive cannot interact in the same vertex as in Fig. 2(b) since they act on perpendicular directions, while the contribution of two quench pulses, which provides a peak at a frequency of $-2\Delta_0$ [as in Fig. 2(d)], can still take place.

APPENDIX D: SYMMETRIC GAUSSIAN-SHAPED DRIVING PULSE

Here, we repeated the same calculations of the nonlinear current generation in the quench-drive spectroscopy setup as in the main text, but using a symmetric Gaussian envelope for the drive pulse. The results are shown in Figs. 12 and 13 and correspond to those in Figs. 5–8 in the main text, where the asymmetric drive was used. In the top panel of Fig. 13, the equilibrium high-harmonic generation does not include the shoulder peak at $\omega = 2\Delta + \omega_d$, $\omega_{\Delta t} = 0$, since it was generated by the initial effective quench of the asymmetric driving field. However, all other features of high-harmonic modulation and transient excitation at $\omega_{\Delta t} = 2\Delta$ are still present, since they originate from the wave mixing of the quench and the drive pulses, independently of their shape.

[1] C. Varma, Higgs boson in superconductors, J. Low. Temp. Phys. **126**, 901 (2002).

[2] D. Pekker and C. Varma, Amplitude/Higgs modes in condensed matter physics, Annu. Rev. Condens. Matter Phys. **6**, 269 (2015).

[3] N. Tsuji and H. Aoki, Theory of Anderson pseudospin resonance with Higgs mode in superconductors, Phys. Rev. B **92**, 064508 (2015).

[4] A. Kumar and A. F. Kemper, Higgs oscillations in time-resolved optical conductivity, Phys. Rev. B **100**, 174515 (2019).

[5] F. Giorgianni, T. Cea, C. Vicario, C. P. Hauri, W. K. Withanage, X. Xi, and L. Benfatto, Leggett mode controlled by light pulses, Nat. Phys. **15**, 341 (2019).

[6] R. Shimano and N. Tsuji, Higgs mode in superconductors, Annu. Rev. Condens. Matter Phys. **11**, 103 (2020).

[7] L. Schwarz and D. Manske, Theory of driven higgs oscillations and third-harmonic generation in unconventional superconductors, Phys. Rev. B **101**, 184519 (2020).

[8] M. A. Müller, P. A. Volkov, I. Paul, and I. M. Eremin, Collective modes in pumped unconventional superconductors with competing ground states, Phys. Rev. B **100**, 140501(R) (2019).

[9] M. A. Müller and I. M. Eremin, Signatures of Bardasis-Schrieffer mode excitation in third-harmonic generated currents, Phys. Rev. B **104**, 144508 (2021).

[10] L. Schwarz, B. Fauseweh, N. Tsuji, N. Cheng, N. Bittner, H. Krull, M. Berciu, G. S. Uhrig, A. P. Schnyder, S. Kaiser, and D. Manske, Classification and characterization of nonequilibrium Higgs modes in unconventional superconductors, Nat. Commun. **11**, 287 (2020).

[11] F. Gabriele, M. Udina, and L. Benfatto, Non-linear terahertz driving of plasma waves in layered cuprates, Nat. Commun. **12**, 752 (2021).

[12] H. Chu, M.-J. Kim, K. Katsumi, S. Kovalev, R. D. Dawson, L. Schwarz, N. Yoshikawa, G. Kim, D. Putzky, Z. Z. Li *et al.*, Phase-resolved Higgs response in superconducting cuprates, Nat. Commun. **11**, 1 (2020).

[13] N. R. Poniatowski, J. B. Curtis, A. Yacoby, and P. Narang, Spectroscopic signatures of time-reversal symmetry breaking superconductivity, Commun. Phys. **5**, 44 (2022).

[14] T. Kamatani, S. Kitamura, N. Tsuji, R. Shimano, and T. Morimoto, Optical response of the Leggett mode in multiband superconductors in the linear response regime, Phys. Rev. B **105**, 094520 (2022).

[15] T. Cea, C. Castellani, and L. Benfatto, Nonlinear optical effects and third-harmonic generation in superconductors: Cooper pairs versus Higgs mode contribution, Phys. Rev. B **93**, 180507(R) (2016).

[16] M. Puviani, L. Schwarz, X.-X. Zhang, S. Kaiser, and D. Manske, Current-assisted Raman activation of the Higgs mode in superconductors, Phys. Rev. B **101**, 220507(R) (2020).

[17] R. Matsunaga, Y. I. Hamada, K. Makise, Y. Uzawa, H. Terai, Z. Wang, and R. Shimano, Higgs Amplitude Mode in the BCS Superconductors Nb$_{1-x}$Ti$_x$N Induced by Terahertz Pulse Excitation, Phys. Rev. Lett. **111**, 057002 (2013).

[18] K. Katsumi, N. Tsuji, Y. I. Hamada, R. Matsunaga, J. Schneeloch, R. D. Zhong, G. D. Gu, H. Aoki, Y. Gallais, and R. Shimano, Higgs Mode in the *d*-Wave Superconductor Bi$_2$Sr$_2$CaCu$_2$O$_{8+x}$ Driven by an Intense Terahertz Pulse, Phys. Rev. Lett. **120**, 117001 (2018).

[19] R. Matsunaga, N. Tsuji, K. Makise, H. Terai, H. Aoki, and R. Shimano, Polarization-resolved terahertz third-harmonic generation in a single-crystal superconductor NbN: Dominance of the Higgs mode beyond the BCS approximation, Phys. Rev. B **96**, 020505(R) (2017).

[20] B. Mansart, J. Lorenzana, A. Mann, A. Odeh, M. Scarongella, M. Chergui, and F. Carbone, Coupling of a high-energy excitation to superconducting quasiparticles in a cuprate from coherent charge fluctuation spectroscopy, Proc. Natl. Acad. Sci. USA **110**, 4539 (2013).

[21] S. T. Cundiff and S. Mukamel, Optical multidimensional coherent spectroscopy, Phys. Today **66**(7), 44 (2013).

[22] M. Woerner, W. Kuehn, P. Bowlan, K. Reimann, and T. Elsaesser, Ultrafast two-dimensional terahertz spectroscopy of elementary excitations in solids, New J. Phys. **15**, 025039 (2013).

[23] J. Lu, X. Li, H. Y. Hwang, B. K. Ofori-Okai, T. Kurihara, T. Suemoto, and K. A. Nelson, Coherent Two-Dimensional Terahertz Magnetic Resonance Spectroscopy of Collective Spin Waves, Phys. Rev. Lett. **118**, 207204 (2017).

[24] F. Mahmood, D. Chaudhuri, S. Gopalakrishnan, R. Nandkishore, and N. P. Armitage, Observation of a marginal Fermi glass, Nat. Phys. **17**, 627 (2021).

[25] Y. Wan and N. P. Armitage, Resolving Continua of Fractional Excitations by Spinon Echo in THz 2D Coherent Spectroscopy, Phys. Rev. Lett. **122**, 257401 (2019).

[26] M. Udina, T. Cea, and L. Benfatto, Theory of coherent-oscillations generation in terahertz pump-probe spectroscopy: From phonons to electronic collective modes, Phys. Rev. B **100**, 165131 (2019).

[27] H. P. Ojeda Collado, G. Usaj, C. A. Balseiro, D. H. Zanette, and J. Lorenzana, Emergent parametric resonances and time-crystal phases in driven Bardeen-Cooper-Schrieffer systems, Phys. Rev. Res. **3**, L042023 (2021).

[28] T. Cea, C. Castellani, G. Seibold, and L. Benfatto, Non-relativistic Dynamics of the Amplitude (Higgs) Mode in Superconductors, Phys. Rev. Lett. **115**, 157002 (2015).

[29] T. Cea and L. Benfatto, Signature of the Leggett mode in the A_{1g} raman response: From MgB_2 to iron-based superconductors, Phys. Rev. B **94**, 064512 (2016).

[30] R. Haenel, P. Froese, D. Manske, and L. Schwarz, Time-resolved optical conductivity and Higgs oscillations in two-band dirty superconductors, Phys. Rev. B **104**, 134504 (2021).

[31] L. Schwarz, R. Haenel, and D. Manske, Phase signatures in the third-harmonic response of Higgs and coexisting modes in superconductors, Phys. Rev. B **104**, 174508 (2021).

[32] M. Silaev, Nonlinear electromagnetic response and Higgs-mode excitation in BCS superconductors with impurities, Phys. Rev. B **99**, 224511 (2019).

[33] Y. Murotani and R. Shimano, Nonlinear optical response of collective modes in multiband superconductors assisted by non-magnetic impurities, Phys. Rev. B **99**, 224510 (2019).

[34] G. Seibold, M. Udina, C. Castellani, and L. Benfatto, Third harmonic generation from collective modes in disordered superconductors, Phys. Rev. B **103**, 014512 (2021).

[35] N. Tsuji and Y. Nomura, Higgs-mode resonance in third harmonic generation in NbN superconductors: Multiband electron-phonon coupling, impurity scattering, and polarization-angle dependence, Phys. Rev. Res. **2**, 043029 (2020).

[36] Z.-X. Wang, J.-R. Xue, H.-K. Shi, X.-Q. Jia, T. Lin, L.-Y. Shi, T. Dong, F. Wang, and N.-L. Wang, Transient Higgs oscillations and high-order nonlinear light-Higgs coupling in a terahertz wave driven NbN superconductor, Phys. Rev. B **105**, L100508 (2022).

[37] F. Yang and M. W. Wu, Gauge-invariant microscopic kinetic theory of superconductivity: Application to the optical response of Nambu-Goldstone and Higgs modes, Phys. Rev. B **100**, 104513 (2019).

[38] P. W. Anderson, Random-phase approximation in the theory of superconductivity, Phys. Rev. **112**, 1900 (1958).

[39] Y. Nambu, Quasi-particles and gauge invariance in the theory of superconductivity, Phys. Rev. **117**, 648 (1960).

[40] H. P. O. Collado, N. Defenu, and J. Lorenzana, Engineering Higgs dynamics by spectral singularities, arXiv:2205.06826.

[41] M. Puviani and D. Manske, Quench-drive spectroscopy of cuprates, Faraday Discuss. **237**, 125 (2022).

[42] C. Giannetti, New perspectives in the ultrafast spectroscopy of many-body excitations in correlated materials, Nuovo Cimento C **39**, 279 (2016).